Available online at www.sciencedirect.com
SCIENCE DIRECT
Thin Solid Films 474 (2005) 133–140
thin solid films
www.elsevier.com/locate/tsf

Use of low-temperature nanostructured CuO thin films deposited by spray-pyrolysis in lithium cells

J. Morales[a], L. Sánchez[a,*], F. Martín[b], J.R. Ramos-Barrado[b], M. Sánchez[b]

[a]*Departamento de Química Inorgánica e Ingeniería Química, Facultad de Ciencias, Campus de Rabanales, Edificio Marie Curie, Universidad de Córdoba, 14071 Córdoba, Spain*
[b]*Laboratorio de Materiales y Superficie (Unidad Asociada al CSIC), Universidad de Málaga, Spain*

Received 26 February 2004; received in revised form 2 July 2004; accepted 22 August 2004
Available online 18 September 2004

Abstract

Nanostructured CuO thin films were prepared by spray pyrolysis of aqueous copper acetate solutions at temperatures over 200–300 °C range. The textural and structural properties of the films were determined by scanning electron microscopy, atomic force microscopy, X-ray diffraction spectroscopy and X-ray photoelectron spectroscopy (XPS). Although the sole crystalline phase detected in the film was CuO, XPS spectra revealed a more complex surface structure due to the presence of undecomposed copper acetate that can be easily removed by Ar^+ ion sputtering. The heating temperature was found to have little limited effect on the particle size and thickness of the films, which, however, increased significantly increasing deposition time. The film with the smallest grain size exhibited an excellent electrochemical response in Li battery electrodes and was capable of supplying sustained specific capacity as high as 625 A h kg^{-1} (50% greater than that delivered by bulk CuO and close to the theoretical capacity for the CuO⇔Cu reaction) upon extensive cycling.

PACS: 68.55.-a
Keywords: Copper oxide; Thin films; Spray pyrolysis; Lithium batteries

1. Introduction

Copper oxide-based materials are of interest on account of their potential uses in many technological fields. CuO and Cu_2O materials are known to be p-type semiconductors in general and hence potentially useful for constructing junction devices such as pn junction diodes [1]. Apart from their semiconductor applications, these materials have been employed as heterogenous catalysts for several environmental processes [2,3], solid state gas sensor heterocontacts [4,5], and microwave dielectric materials [6]. Their use in power sources has received special attention. Thus, in addition to photovoltaic devices [7,8], copper oxides have been used as electrode materials for lithium batteries. The earliest studies in this area focused on their potential use as cathodes in lithium primary cells [9,10]. Recently, their ability to reversibly react with Li ions at low potential values was ascribed to the following reaction [11]:

$$Cu_nO + 2Li \Leftrightarrow nCu + Li_2O \quad (1)$$

The theoretical deliverable specific capacity of CuO is 675 A h kg^{-1}, which is much higher than that of graphite-based anodic materials (the theoretical gravimetric capacity for which is 372 A h kg^{-1}). For this reason, CuO has been proposed as candidate to replace these carbonaceous materials as negative electrodes in Li-ion batteries. In practice, however, bulk CuO electrodes deliver a sustained reversible capacity of ca. 400 A h kg^{-1} [12], so roughly 40% of the CuO theoretical capacity, referred to its reduction to Cu, is unusable.

Nanostructured materials have emerged as attractive alternatives to conventional materials by virtue of their prominent electronic and chemical properties [13]. Recently, we reported nanostructured PbO_2 and Ag thin electrodes to exhibit excellent electrochemical activity as electrodes in

* Corresponding author. Tel.: +34 957 218620; fax: +34 957 218621.
E-mail address: luis-sanchez@uco.es (L. Sánchez).

0040-6090/$ - see front matter © 2004 Elsevier B.V. All rights reserved.
doi:10.1016/j.tsf.2004.08.071

lead-acid cells [14] and lithium batteries [15], respectively. We extended the methodology used with these electrodes to CuO with the aim of improving its electrochemical response in lithium cells. In this work, we report the preparation and characterization of nanocrystalline CuO thin films by spray pyrolysis of an aqueous solution of copper acetate as a simple preparation method that requires no sophisticated equipment. X-ray diffraction (XRD) spectroscopy, electron and atomic force microscopy and X-ray photoelectron spectroscopy (XPS) were used for characterization purposes. We also explored the activity of a selected film as electrode in lithium batteries. This electrode preparation procedure results increases the electrochemical reactivity of CuO relative to bulk material.

2. Experimental details

A spray pyrolysis method described elsewhere [16] was used to prepare the CuO thin films. An aqueous solution of 0.05 M $Cu(CH_3COO)_2$ was used as precursor. The solution was pumped into the air stream in the spray nozzle at a rate of 50 ml h^{-1} by means of a syringe pump, for a preset time of 30, 60 for 80 min. An air stream of 25 l min^{-1}, measured at 1.25 bar, was used to atomize the solution. Circular disks of commercial 304 stainless steel (0.4 mm thick and 7.5 mm in diameter) were used as substrates. The disks were kept at temperatures over the range 200–300 °C. The amount of oxide film attached to the substrate was determined by weighting the electrode before and after deposition, using a Sartorius microbalance with ±1 μg sensitivity.

X-ray diffraction patterns were recorded on a Siemens D5000 X-ray diffractometer, using Cu Kα radiation an a graphite monochromator, in steps of 0.02° and 1.2 s. Scanning electron microscopy (SEM) images were obtained on a Jeol JMS-5300 microscope. Topographic atomic force microscopy (AFM) examinations were performed by using a Nanoscope IIIa contact-mode AFM (Digital Instruments). Type NP cantilevers (Digital Instruments) with Si_3N_4 tips and a spring constant of 0.58 N/m were employed.

X-ray photoelectron and X-ray excited Auger spectra were obtained with a Physical Electronics PHI 5700 spectrometer using non-monochromated MgKα radiation ($h\nu$=1253.6 eV) and a hemispherical analyser operating at constant pass energy of 29.35 eV. The spectra were recorded with the X-ray generator operating at 15 kV and 20 mA. The energy scale of the spectrometer was calibrated using the Cu 2p3/2, Ag 3d5/2 and Au 4f7/2 photoelectron lines at 932.7, 368.3 and 84.0 eV, respectively. The vacuum in the analysis chamber was better than 10^{-9} mbar.

Binding energies were corrected using the binding energy values for C 1s of adventitious carbon (and for the methyl group) at 284.8 eV. Samples were mounted on a holder without adhesive tape and kept under high vacuum in the preparation chamber overnight before they were transferred to the analysis chamber of the spectrometer. Survey spectra over the range 0–1200 eV were recorded at a 187.85 pass energy, each region being scanned several times to ensure an adequate signal-to-noise ratio. A 3×3-mm sample area was sputtered with 4 keV Ar^+; the sputter rate was assumed to be ~0.3 nm min^{-1} as determined for Ta_2O_5 under identical sputter conditions. Spectra were processed using PHI-Access V.6 and Multipak software, both from Physical Electronics. High-resolution spectra were fitted upon Shirley background correction and satellite subtraction. Surface atomic concentrations were determined from peak areas, using Shirley background subtraction and sensitivity factors provided by the spectrometer manufacturer (Physical Electronics, Eden Prairie, MN). Data for the Cu 2p region were acquired at short times in order to minimize the reduction of copper oxide by X-rays.

Electrochemical measurements were carried out in two-electrodes cell, using lithium as counter-electrode. The electrolyte used was Merck battery electrolyte LP 40, which consists of 1 M $LiPF_6$ in ethylene carbonate and dimethyl carbonate in 1:1 w/w ratio. Circular disks of stainless steel coated with the active material were used as working electrodes. Cells were galvanostatically charged and discharged at a current density of 0.075 mA mg^{-1}. SPES curves were recorded at 75 mV h^{-1} per step. All electrochemical measurements were controlled via a MacPile II potentiostat−galvanostat.

3. Results and discussion

The experimental conditions used to prepare films are shown in Table 1. The amount of film deposited increased with increasing deposition time; no clear-cut correlation with the deposition temperature was observed, however. All samples thoroughly coated with substrate; however, film uniformity varied with temperature, as revealed by the SEM images. Fig. 1 shows selected typical images for the samples. Samples A, B and C were rougher than the other because the small amounts of deposited material allowed the wrinkled morphology of the substrate surface to be distinguished. Increasing the time of deposition (samples E and F) led to a dense, compact homogeneous film coating and the formation of some cracks in parallel to the increase in the amount deposited. However, sample D, which was

Table 1
Preparation conditions and selected properties of CuO thin films

Film	Temperature (°C)	Time (min)	Mass deposited (mg cm^{-2})	Thickness[a] (nm)
Sample A	200	30	0.36	660
Sample B	250	30	0.30	475
Sample C	300	30	0.17	420
Sample D	200	60	0.58	1100
Sample E	250	60	0.56	1150
Sample F	300	80	0.73	1250

[a] Values estimated from SEM images.

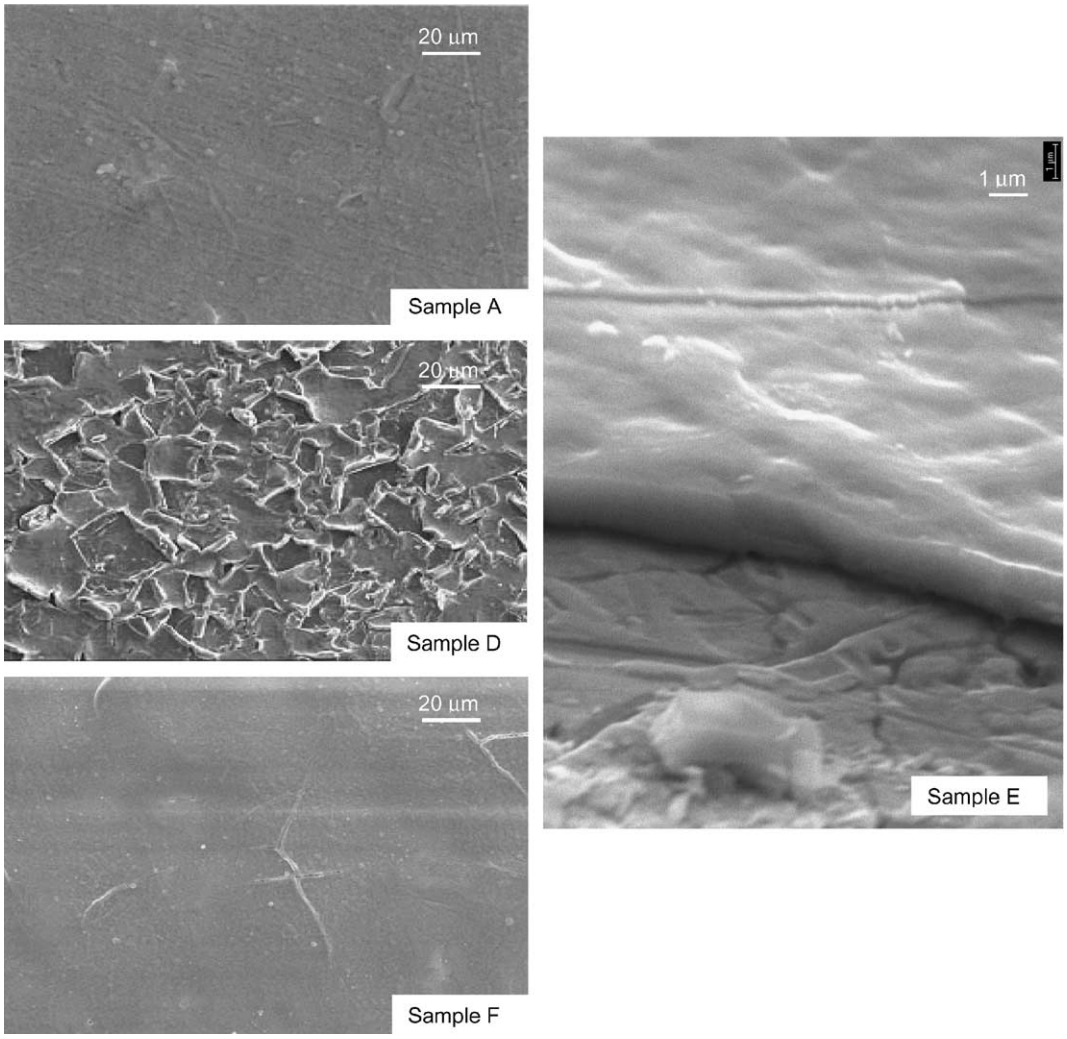

Fig. 1. SEM images of various CuO thin films.

obtained at 200 °C, exhibited a highly cracked surface. This different morphology could be explained as follows. At the lowest deposition temperatures, while the film was growing, a substantial amount of undecomposed organic precursor remained in the film. By the end of the growing process, nearly the whole organic component had been degraded and converted into copper oxide. The difference in density between the mixture of undecomposed acetate and copper oxide resulted in poor adherence to the substrate and in peeling of the film. At higher temperatures, the copper oxide film was directly formed on the substrate, so it exhibited good adherence and no cracks. However, if the deposition time was increased, the resulting compact film was thicker and subject to internal stress and strain as a result of the metal substrate contracting upon cooling, among other factors. Cracks can appear at some "weak" points in the film that progress through film releasing stress.

Film thickness was estimated from cross-sectional SEM images such as that of Fig. 1; the results are shown in Table 1. Particle size was calculated by averaging the results of several AFM observations in different regions of the films (Fig. 2). The increased surface resolution of this microscopic technique revealed films to consist of clusters of round-shaped grains. Fig. 3 shows the particle size distribution for the different samples as determined from the AFM images.. Both film thickness and crystal size distribution increased with increasing deposition time, on equal deposition time, however, the temperature seemingly had little influence on both parameters. Except for sample F, calculating the crystallite size from XRD patterns was impossible owing to the low peak-to-background ratio. By applying the Scherrer equation to the (111) reflection, a value of ca. 10 nm was obtained. Such a value is much smaller than the particle size calculated from AFM images, which suggests that grains are formed by several diffraction domains.

Probably, the low temperature used to prepare these films accounts for the difference and their nanometric nature, particularly at short deposition times (30 min). It is worth noting the more uneven size distribution of sample D, the SEM image for which also exhibited a different surface morphology.

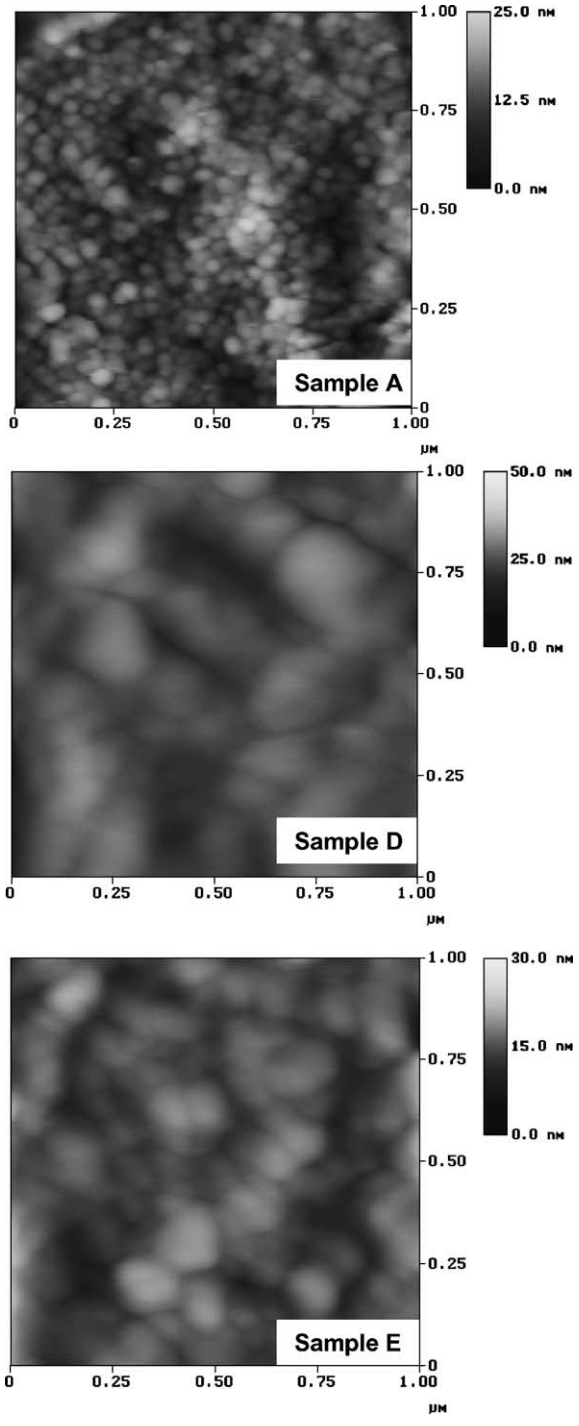

Fig. 2. AFM images of selected CuO thin films.

The XRD patterns for the films are shown in Fig. 4. The low signal-to-noise ratio obtained is consistent with the low crystallinity of the samples. Two main signals at 35.6° and 38.7°2θ were apparent in the XRD patterns that were ascribed to the (−111) and (111) reflections of the CuO phase [17]. Peak intensities, and hence crystallinity, increased with increasing temperature and, especially, increasing deposition time. Although the low particle crystallinity reflected in the substantial peak observed precluded the accurate identification of the Cu_2O phase in the films, the absence of the (111) reflection located at a rather different spacing from those for CuO rules out its formation under the deposition conditions used.

Supplementary data for the surface characterization of these films were obtained from XPS measurements. Fig. 5 shows the Cu 2p, O 1s and C 1s surface XPS spectra for samples A, B and C, no other signals belonging to Fe, Cr or Ni, which are major constituent elements of the substrate were detected, which provides thorough, additional evidence of the homogeneous coating of the substrate. The well-defined shake-up satellite structures observed at about 7 and 9.5 eV on the high binding energy side of the copper core line $2p_{3/2}$ (centred at 934 eV) is typical of Cu^{2+} species and due to multiplet splitting. Moreover, the Cu $L_3M_{4.5}M_{4.5}$ Auger signal centred at a kinetic energy of 917.8 eV [18] is also consistent with the presence of Cu^{2+} as the dominant species on the surface. However, the Cu $2p_{1/2}$ and $2p_{3/2}$ peaks are relatively broad and seem to be influenced by the presence of Cu_2O and/or other copper species (e.g. residual copper acetate). In addition, the C and O 1s peaks exhibit different components, so these atoms must lie in different chemical environments.

In order to acquire a more precise knowledge of these environments, peaks were fitted using a Gaussian/Lorentzian mixed function. The Cu $2p_{3/2}$ peak profiles (Fig. 6a and d) were fitted with two contributions assigned to CuO (933.7 eV [19], curve 2), Cu_2O (932.5 eV [19], curve 1), and a third with its maximum at 935.6 eV (curve 3). This

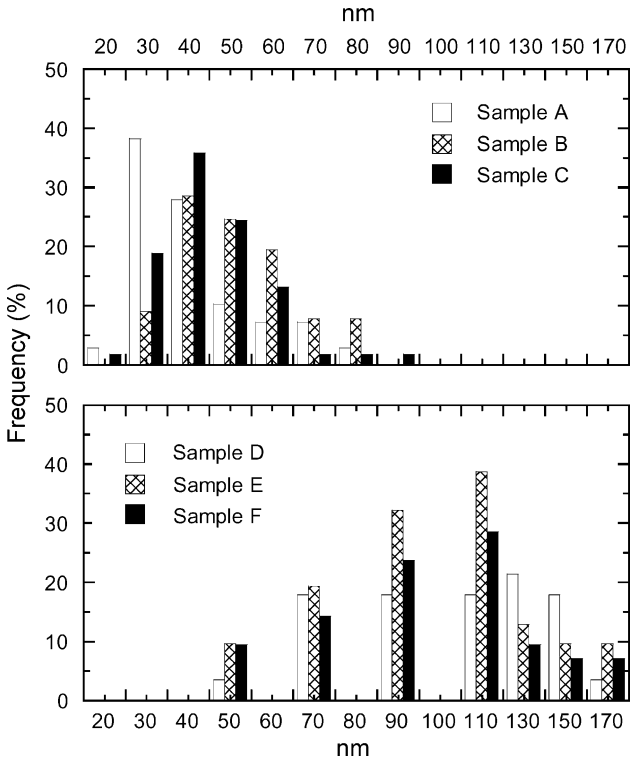

Fig. 3. Particle size distribution of CuO films as calculated from AFM images.

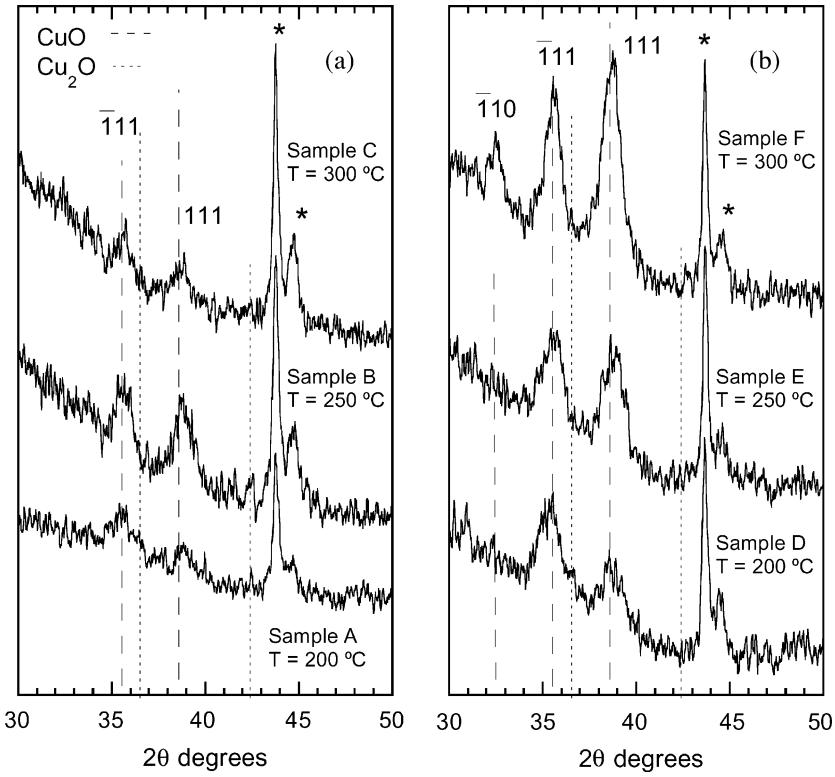

Fig. 4. XRD patterns for CuO thin films. [*: Diffraction lines corresponding to the substrate.]

latter peak can be assigned to either undecomposed acetate (the reported signal for this compound spans the range 931.8–935.1 eV [19]) or hydroxylated species such as $Cu(OH)_2$ (BE 934.4–935.1 eV [19]). Curves 4 and 5 in Figs. 5a and 6d, represent the Cu $2p_{3/2}$ satellite contributions. The fitted curve for the C1s photoemission (Fig. 6b and e) exhibited three contributions. The peaks at 284.8 (curve 1) and 286.2 eV (curve 2) were attributed to C–H/C–C and C–O, respectively, and due to the methyl group and adventitious carbon. The peak at 288.3 eV (curve 3) was assigned to the O=C–O in acetate ion. Therefore, some undecomposed acetate is present at the film surface. The intensity of this peak decreased as the deposition temperature increased, whereas that of peaks 2 and 3 in the Cu $2p_{3/2}$ profiles

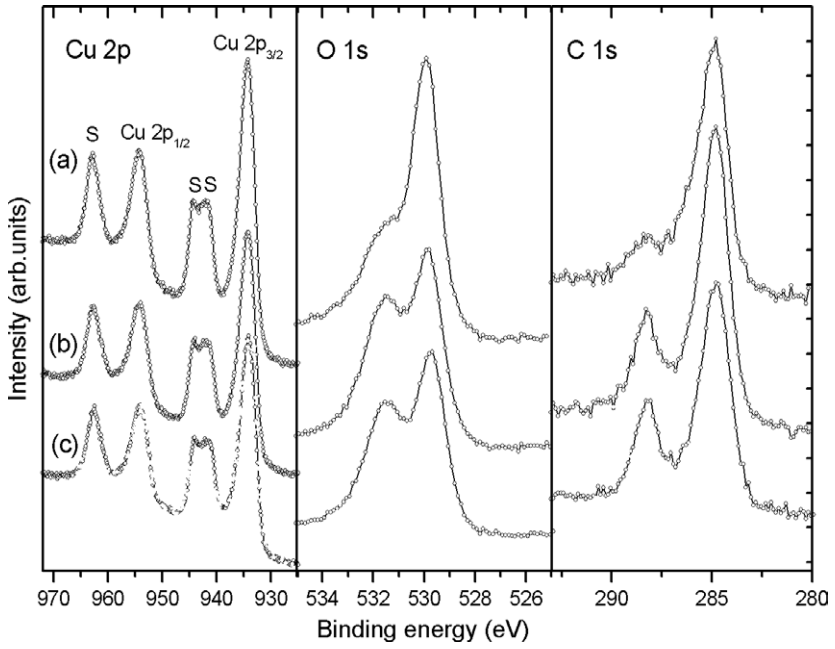

Fig. 5. XPS Cu 2p, O 1s and C 1s core level spectra belonging to the following samples: (a) A, (b) B, (c) C.

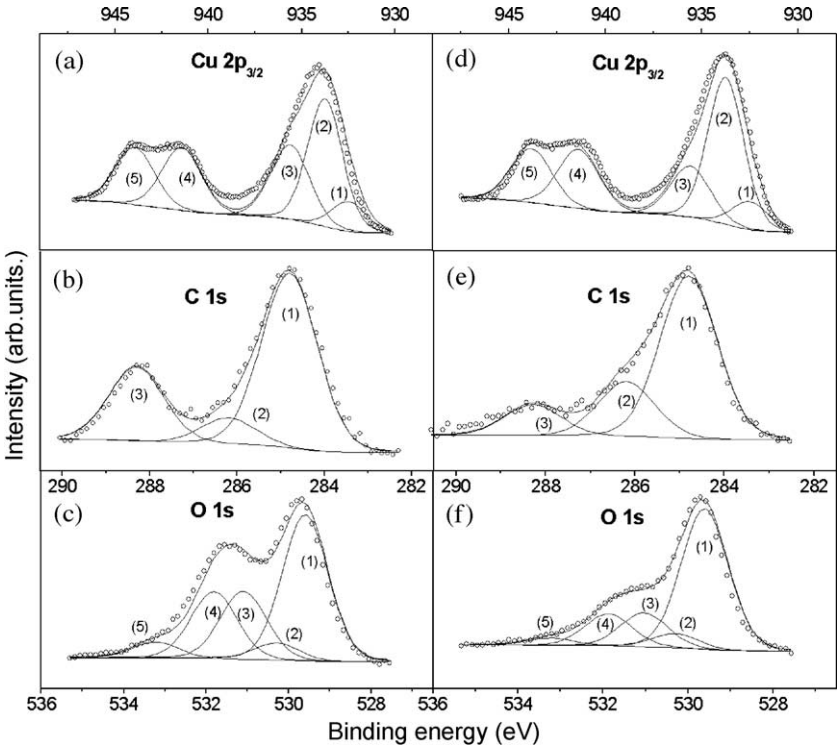

Fig. 6. Fitted profiles for Cu $2p_{3/2}$, O1s and C 1s core level spectra corresponding to samples A (a, b, c) and C (d, e, f).

increased and decreased, respectively, with increasing temperature. This provides further support for the presence of undecomposed acetate at the film surface and for assignation of the component at 935.6 eV in the Cu profile to this species. The intensity of peak 1 for Cu $2p_{3/2}$ (Fig. 6a) changed little with the deposition time or temperature, so the Cu_2O content is scarcely affected by these variables as it arises from the reduction of Cu^{2+} by X-rays [20]. The fitted O 1s signal is rather complex, with many components corresponding to various chemical states. The peak profile was fitted to five components as shown in Figs. 6c and f. The peaks at 529.6 and 530.3 eV were assigned to CuO (curve 1) and Cu_2O (curve 2), respectively. The others could be assigned to traces of undecomposed copper acetate and water-containing species. Thus, the peak at 531.2 eV (curve 3) can be assigned to hydroxyl groups and the other two, curves 4 and 5, to oxygen atoms in the carboxyl group. As expected, the intensity of these latter peaks also decreased with increasing deposition temperature.

Based on the above-described results, Cu^{2+} is the dominant oxidation state at the film surface; part of it is present as undecomposed copper acetate—particularly at the lower deposition temperatures. However, the layer of undecomposed material is indeed very thin, as shown by the spectra obtained after 0.3 min of Ar^+ ion sputtering. The most salient changes in these spectra were as follows: (i) the C1s peak almost disappeared—the atomic concentration dropped to 3–4% (see Table 2); (ii) the O1s peak was markedly more symmetric, without the shoulder at 531.5 eV, and the content calculated from it was considerably lower; (iii) the Cu 2p profile underwent significant shifts. The shake-up satellite structure of Cu^{2+} virtually disappeared and the 2p doublet shrank. Now, the $2p_{3/2}$ line was located at 932.5 eV, a typical value for Cu(I) species. Moreover, the copper content was significantly higher (nearly twice higher than that of oxygen). This means that the surface composition approaches that of Cu_2O as a consequence of the instability of Cu^{2+} species to Ar^+ ion bombardment and its transformation into cuprite.

Based on the similar morphology and composition of the nanometric CuO, we selected sample A, which contained an increased amount of mass deposited, for electrochemical tests. Fig. 7a shows the first galvanostatic discharge–charge curve and the second discharge curve for Li/Sample A cell. The first discharge curve exhibits an abrupt drop in the potential up to 1.4 V, with a small slope change below 2.5 V that is followed by two *pseudo-plateaux* centred at ca. 1.3 and 0.9 V. The plateaux are even better defined in the second discharge curve. Below 0.7 V, the potential tends to

Table 2
XPS elemental analysis (%) of the six thin films obtained

Film	C	O	Cu
Sample A	23 (3.5)	43 (29.5)	34 (67)
Sample B	25 (3.0)	42 (29.0)	33 (68)
Sample C	19 (4.5)	43 (30.5)	38 (65)
Sample D	28 (3.5)	42 (29.5)	30 (67)
Sample E	42 (3.0)	38 (29.0)	20 (38)
Sample F	33 (4.5)	39 (30.5)	28 (65)

The values in brackets were obtained upon ion-etching for 20 s.

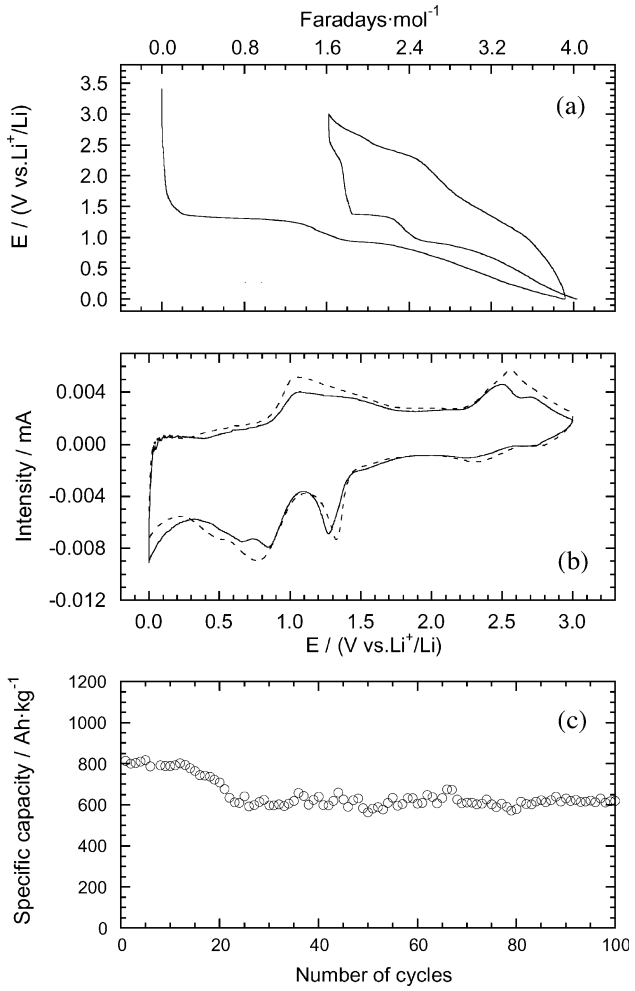

Fig. 7. (a) First galvanostatic curves, (b) SPES curves and (c) cycling properties of Li/sample A cell.

decrease gradually as the discharge depth increases, with a slope change below 0.5 V. The voltage curve profile resemble those reported for bulk CuO [12,21].

The first discharge curve for the Li/CuO thin film cell considerably exceeds the nominal capacity of the electrode—two lithium ions per mole of compound for the theoretical CuO→Cu reduction process; this can be ascribed to the electrolyte being reduced at potentials below 0.5 V. The presence of impurities of other transition metals accounting for the abnormal first discharge capacity observed can be discarded in the light of the XPS results. The participation of the electrolyte in the overall electrochemical process seems to play a major role. The formation of a solid electrolyte interface (SEI) has been suggested for these types of electrodes when discharged at low potentials. The presence of an SEI-like layer involving the metallic particles can be ascribed to their catalytic activity. Thus, the metallic nanograin surface may activate the solvent molecules and facilitate the charge transfer needed for redox processes, and favouring their reversibility [22]. The electrode exhibits a high electrolyte/active material ratio that may facilitate the electrolyte reduction. Indeed, a similar discharge curve profile has been found for Cu_2O anode material grown on Ti-plated quartz crystals; the first potential drop was ascribed to the reduction of electrolyte components via a reaction such as [22]

$$EC + 2e^- + 2Li^+ \Leftrightarrow Li_2CO_3 + \text{alkane or alkene} \quad (2)$$

Direct evidence of partial electrolyte decomposition was obtained from the XPS spectra of Fig. 8. When the cell was discharged to 0.0 V, the main changes detected were in the C 1s emission line, which exhibited a new peak at 289.8 eV assigned to carbonate ion formed in the previous reaction.

The charge curve exhibited strong polarization, with subtle slope changes. The slope change observed above 1.5 V in the charge curve could be ascribed to a different Li-driven electrochemical process. The cell tended to remove about two Li^+ ions per unit formula at a cut-off voltage of 3.0 V, which is consistent with the value reported for CuO bulk material and corresponding to the Cu→CuO oxidation process [21].

The reversibility of the electrochemical processes was demonstrated by using the step potential electrochemical spectroscopy (SPES) technique (Fig 7b). Taking into account that the amount of lithium removed in the first charge was similar to that inserted in the second discharge (Fig. 7a), the discussion of the SPES curves will be restricted to such processes. The most salient feature of the first anodic curve was the presence of two doublets centred at 1.2 and 2.6 V. The second cathodic curve exhibited a weak peak at 2.35 V followed by a stronger band at 1.3 V and two broad overlapping peaks at 0.85 and 0.55 V. As reported in Ref. [21], the curve shape reflects the following redox processes: CuO⇔Cu_2O (1.3, 2.7 V), Cu_2O⇔Cu (0.85, 2.5 V) and the reduction–oxidation of the electrolyte (0.5, 1.25 V). The cathodic peak at 2.35 V has been ascribed to a lithium insertion process in the CuO phase [20]. Further cycling hardly changed the curve

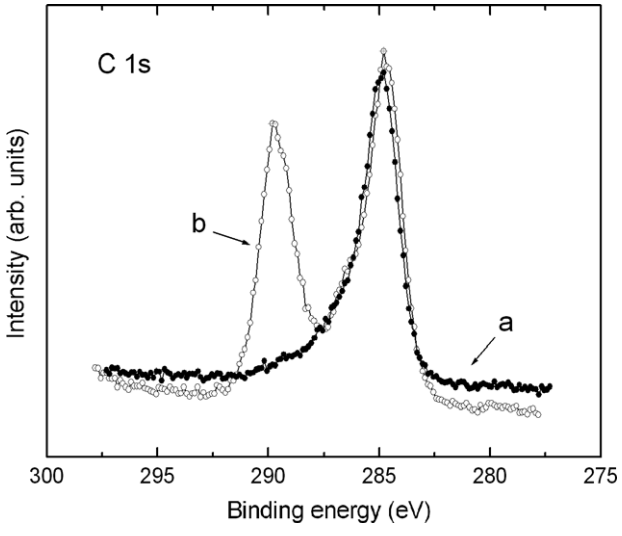

Fig. 8. C 1s core level spectra for film A impregnated with electrolyte (a) and after discharge at 0.0 V (b).

profiles, so the redox processes involved in the anodic and cathodic scans can be assumed to be reversible.

Fig. 7c shows the electrochemical response of Sample A on cycling. As stated above, the specific capacity delivered was initially higher than the theoretical value (674 A h kg^{-1}) due to the electrolyte participation in the electrochemical process—particularly during the first few cycles. The cell has the ability to deliver a nearly constant specific capacity of 625 A h kg^{-1} over 100 cycles. In order to justify this value, one must accept the presence of Cu^{2+} after the cell is charged, as well as the following reversible reaction:

$$CuO + 2Li \Leftrightarrow Cu + Li_2O. \quad (3)$$

The cycling properties of these CuO thin films electrodes are different from those reported for bulk CuO [12]. Thus, the discharge capacity delivered by this later system on cycling is ca. 400 A h kg^{-1} and thus only slightly greater than the theoretical value for Cu_2O (375 A h kg^{-1}). Therefore, the oxidation reaction $Cu^{+} \rightarrow Cu^{2+}$ is kinetically hindered in the bulk material and the electrochemical process on cycling is essentially controlled by the Cu_2O/Cu pair. The improved electrochemical performance of CuO film relative to bulk CuO can be ascribed to two factors. First, the nanometric nature of particles increases the electrochemical activity of the film. Second, the small thickness and good contact of the film with the substrate facilitate electron transfers between the active material and substrate, which acts as a current collector. Electrode preparation method therefore has an advantage over the conventional pellets system: the electrode can deliver a high capacity on prolonged cycling without the need for additives such as electronic conductors (e.g. carbon black) or binders.

Acknowledgements

This work was supported by Junta de Andalucía (Group FQM-175) and Ministerio de Ciencia y Tecnología (Project MAT2002-04477-C02-02).

References

[1] M. Muhibbullah, M.O. Hakim, M.G.M. Choudhury, Thin Solid Films 423 (2003) 103.
[2] J.R. Ortiz, T. Ogura, J. Medina-Valtierra, S.E. Acosta-Ortiz, P. Bosh, J.A. de las Reyes, V.H. Lara, Appl. Surf. Sci. 174 (2001) 177.
[3] K.C.C. Kharas, Appl. Catal., B Environ. 2 (1993) 207.
[4] R.B. Vasiliev, M.N. Rumyantseva, N.V. Yakovlev, A.M. Gaskov, Sens. Actuators, B, Chem. 50 (1998) 186.
[5] Y. Nakamura, H. Zhuang, A. Kishimoto, O. Okada, H. Yanagida, J. Electrochem. Soc. 145 (1998) 632.
[6] D.W. Kim, B. Park, J.H. Chung, K.S. Hong, Jpn. J. Appl. Phys. 39 (2000) 2696.
[7] Y.S. Chaudhary, A. Agrawal, R. Shrivastav, V.R. Satsangi, S. Dass, Int. J. Hydrogen Energy 29 (2004) 131.
[8] K.H. Yoon, W.J. Choi, D.H. Kang, Thin Solid Films 372 (2000) 250.
[9] P. Novák, Electrochim. Acta 30 (1985) 1687.
[10] P. Novák, Electrochim. Acta 31 (1986) 1167.
[11] P. Poizot, S. Laruelle, S. Grugeon, L. Dupont, J.M. Tarascon, Nature 407 (2000) 496.
[12] S. Grugeon, S. Laruelle, R. Herrera-Urbina, L. Dupont, P. Poizot, J.M. Tarascon, J. Electrochem. Soc. 148 (2001) A285.
[13] J. Schoonman, Solid State Ionics 5 (2000) 135.
[14] J. Morales, G. Petkova, M. Cruz, A. Caballero, Electrochem. Solid State Lett. 7 (4) (2004) 1.
[15] J. Morales, L. Sánchez, F. Martin, J.R. Ramos-Barrado, M. Sánchez, J. Electrochem. Soc. 151 (2004) 151.
[16] R. Ayouchi, F. Martin, J.R. Ramos-Barrado, M. Martos, J. Morales, L. Sánchez, J. Power Sources 87 (2000) 106.
[17] Powder Diffraction File, Joint Committee on Powder Diffraction Standars, ASTM, Philadelphia, PA, 1989, Card no. 45–937.
[18] B. Timmermans, F. Reiners, A. Hubin, C. Buess-Herman, Appl. Surf. Sci. 144–145 (1999) 54.
[19] J.F. Moulder, W.F. Stickle, P.E. Sool, K.D. Bomber, Handbook of X-ray Photoelectron Spectroscopy, Perkin-Elmer, Eder Prairie, 1992.
[20] E. Cano, C.L. Torres, J.M. Bastisdas, Mater. Corros. 52 (2001) 667.
[21] A. Débart, L. Dupont, P. Poizot, J.B. Leriche, J.M. Tarascon, J. Electrochem. Soc. 148 (2001) A1266.
[22] B. Laik, P. Poizot, J.M. Tarascon, J. Electrochem. Soc. 149 (2002) A251.